crystals

MDPI

Review

Thickness-Dependent Strain Rate Sensitivity of Nanolayers via the Nanoindentation Technique

Jian Song [1], Yue Liu [1,*], Zhe Fan [2,*] and Xinghang Zhang [2]

[1] State Key Laboratory of Metal Matrix Composites, School of Materials Science and Engineering, Shanghai Jiao Tong University, Shanghai 200240, China; songjian2015@126.com

[2] School of Materials Engineering, Purdue University, West Lafayette, IN 47907, USA; xzhang98@purdue.edu

* Correspondence: yliu23@sjtu.edu.cn (Y.L.); zfan.phd@gmail.com (Z.F.)

Received: 14 January 2018; Accepted: 21 February 2018; Published: 9 March 2018

Abstract: The strain rate sensitivity (SRS) and dislocation activation volume are two inter-related material properties for understanding thermally-activated plastic deformation, such as creep. For face-centered-cubic metals, SRS normally increases with decreasing grain size, whereas the opposite holds for body-center-cubic metals. However, these findings are applicable to metals with average grain sizes greater than tens of nanometers. Recent studies on mechanical behaviors presented distinct deformation mechanisms in multilayers with individual layer thickness of 20 nanometers or less. It is necessary to estimate the SRS and plastic deformation mechanisms in this regime. Here, we review a new nanoindentation test method that renders reliable hardness measurement insensitive to thermal drift, and its application on SRS of Cu/amorphous-CuNb nanolayers. The new technique is applied to Cu films and returns expected SRS values when compared to conventional tensile test results. The SRS of Cu/amorphous-CuNb nanolayers demonstrates two distinct deformation mechanisms depending on layer thickness: dislocation pileup-dominated and interface-mediated deformation mechanisms.

Keywords: thin film; nanoindentation; strain rate sensitivity; deformation mechanisms

1. Introduction

For most metallic materials, the plastic deformation can be regarded as a thermally-activated process which can be quantitatively characterized by the values of the strain rate sensitivity (SRS), m, and the dislocation activation volume, V^* [1,2]. SRS is an important indicator of the plasticity of metallic materials, which can be estimated by the amount of activation volume required for dislocation motions. These two inter-related material properties are important for understanding thermally-activated plastic deformation, such as creep.

In general, for crystalline metals, higher values of SRS are often accompanied by excellent ductility and deformability. The values of SRS are strongly size-dependent: for face-centered-cubic (fcc) metals, SRS normally increases with decreasing grain sizes, whereas the opposite holds for body-center-cubic (bcc) structures [3]. Metallic glasses (MGs) exhibit high strength, excellent abrasion and corrosion resistance [4], but they are generally brittle due to the shear band (SB) controlled-deformation mechanisms therefore the SRS is close to zero [5]. Prior studies have shown that adding a crystalline phase to the amorphous matrix can increase the toughness/plasticity of ZrTi-based MGs [6] and crystalline/amorphous (C/A) multilayers [7–14]. For the C/A multilayer composites, their thermally-activated plastic deformation mechanisms can also be revealed by quantifying their SRS. Thus, various methods have been developed for determining SRS in the past few decades [15–22].

The method for determining SRS can be roughly classified as macroscopic testing and "localized" testing, usually nanoindentation. Macroscopically, the SRS is often measured by uniaxial tension [15–20] and compression tests [21,22] on bulk specimens, whereas nanoindentation is widely

adopted to measure SRS of small specimens, such as thin films. Figure 1 illustrates the differences between SRS measurement under tension/compression and nanoindentation. In addition to the different scope of applications, the key difference between uniaxial tension/compression and nanoindentation measurements lies in the determination of strain rate ($\dot{\varepsilon}$). In the tensile/compression testing method, $\dot{\varepsilon}$ is calculated based on the original length of sample (l_o), and its increment (Δl) under displacement-control mode. In comparison, the nanoindentation SRS measurements achieve a constant indentation strain rate $\dot{h}/h$ through maintaining $\dot{P}/P$ based on their relationship (h is the indentation depth, $\dot{h}$ is the displacement rate, P is the loading force, and $\dot{P}$ is the real-time loading rate) [23]. Although the nanoindentation method determines SRS on a local scale, many nanoindentation experiments are typically performed to ensure the results are representative of their overall mechanical properties.

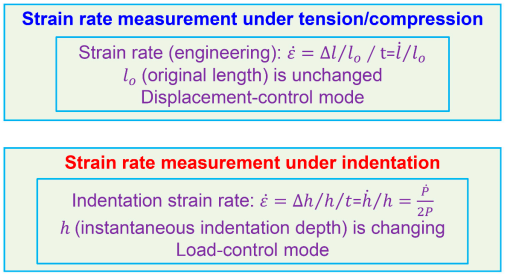

Figure 1. Differences between strain rate sensitivity measurement under tension/compression and nanoindentation. Different from measuring the dimension change of tension and compression specimens, nanoindentation quantifies the strain from a combination of load and indentation depth.

In 1999, the $\dot{P}/P$ technique for SRS measurement was first presented by Lucas and Oliver, and they applied this technique for measuring the hardness of high-purity indium under various strain rates [23]. This method shows good applicability during the high strain rate experiment, however, when it comes to low strain rates, the displacement of the indenter will be significantly affected by thermal drift. In 2010, the continuous stiffness measurement (CSM) that could decrease the influence of thermal drift was proposed by Hay et al. [24]. In 2011, an indentation strain-rate-jump test method for measuring SRS proposed by Maier et al. showed a significant mitigation of the thermal drift [25]. Unlike the previous methods, this special nanoindentation creep method alleviates thermal drift by first applying the highest strain rates and then the lowest strain rates. However, during the strain-rate-jump test, the indentation depths must be greater than 500 nm for reliable determination of SRS.

Recent studies on mechanical behaviors of multilayers focused on deformation mechanisms when the individual layer thickness is 20 nm or less where the majority of multilayer systems reach high strength [26–28]. However, there are limited studies on the size-dependent SRS in multilayers using the nanoindentation test, except some atomistic simulations on the deformation mechanisms of nano-sized thin films [29–32]. Here, we review a new nanoindentation test method that renders hardness nearly insensitive to thermal drift. Such a technique permits reliable determination of SRS for Cu films. The SRS measured using this technique reveals size-dependent variation of deformation mechanisms in Cu/a-CuNb (crystalline Cu/amorphous CuNb) multilayers.

2. Experimental Methods

The 1.5 μm Cu film, 1 μm thick a-CuNb single layer and the Cu/a-CuNb nanolayers with different individual layer thickness (h, ranges from 5 to 150 nm; and total thickness ranges from 1 to 2.4 μm) were deposited on HF-etched Si wafers by DC (direct current) magnetron sputtering. Pure Cu (99.995%) and CuNb alloy (Cu 50 at%-Nb 50 at%) targets were used to prepare these nanostructured materials. The microstructure was characterized by FEI Tecnai G2 F20 TEM (Thermo Fisher Scientific,

Hillsboro, OR, USA). All the nanoindentation tests were conducted on Agilent G200 (Agilent Technologies, Santa Clara, CA, USA) and Hysitron TI950 TriboIndenter (Bruker, Billerica, MA, USA) in the continuous stiffness measurement (CSM) mode. For a-CuNb and Cu/a-CuNb multilayers, at least 10 tests were conducted for each sample at each specific strain rates of 0.2, 0.05, and 0.01 s^{-1}, respectively. For the Cu single-layer, the specific testing strain rates are 0.05, 0.01, and 0.002 s^{-1}.

This new modified testing method developed by Liu et al. [33] involves directly measuring the contact stiffness and calculating the contact area from the measured stiffness and modulus. Figure 2 depicts the differences between the conventional and new modified method. It is easy to find that both the conventional and modified method are based on the relationship performed by Sneddon's stiffness equation [34]:

$$E_r = \frac{\sqrt{\pi}}{2}\frac{S}{\sqrt{A}} \tag{1}$$

where E_r is the reduced elastic modulus, A and S represent the contact area and contact stiffness, respectively [35,36]. The primary difference between these two methods is reflected in the different calculation process of A. As for the conventional method, h (indentation displacement), P (load), and S at different $\dot{\varepsilon}$ can be directly measured, the h_c (contact depth) can be calculated by using the equation:

$$h_c = h - \frac{0.75P}{S} \tag{2}$$

where $0.75P/S$ is a calculated value which represents h_s (the vertical distance from the contact point of the sample and the indenter to the sample surface) [35], then A could be derived by:

$$A = m_0 h_c^2 + m_1 h_c \tag{3}$$

where m_0 and m_1 are determined by the standard calibration process [35]. At last, E_r and H (hardness) could be derived by those parameters. At high strain rates, the measurement error of h is negligible. However, at lower strain rate, the measurement of h will be significantly affected by thermal drift which makes the later calculations become unreliable. Unlike the conventional method, the modified method calculates the contact area from the measured stiffness and modulus, and the process can be summarized as follows: Firstly, measured E_r at high $\dot{\varepsilon}$, then E_r as a known parameter can be used at lower $\dot{\varepsilon}$ later. Secondly, at low $\dot{\varepsilon}$ condition, A can be derived by Equation (1) (thus, H is calculated), then h_c is calculated from Equation (3), and at last, h can be calculated by using the Equation (2). The calculated h instead of directly measured can reduce the thermal-drift effects significantly and control the real-time indentation displacement [33].

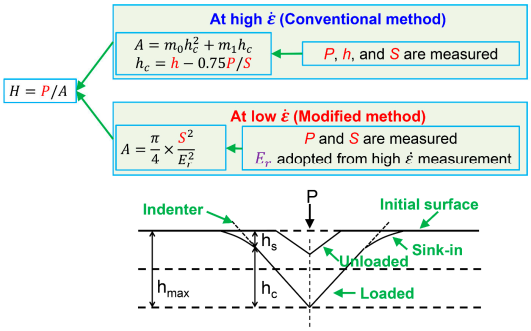

Figure 2. Flowcharts illustrating differences between conventional and modified methods. The conventional method measures h, P, and S at different strain rates ($\dot{\varepsilon}$). Values of h_c, A, E_r, H, and E can be derived. The modified method first determines E_r at high $\dot{\varepsilon}$, then applies E_r as a known parameter at lower $\dot{\varepsilon}$. The h and A value at low $\dot{\varepsilon}$ can be calculated instead of directly measured to reduce the thermal-drift effects.

3. Results and Discussion

The hardnesses of single-layer Cu and a-CuNb films were measured by using this modified method. Figure 3 shows the comparison of nanoindentation results obtained from conventional (blue) and modified (red) methods using the same sets of nanoindentation data at various strain rates. Both the methods show good stability during the high strain rate experiment, and lead to similar results. However, at the lower strain rate, for a-CuNb multilayers (0.01 s^{-1}), the scattering data presented by the conventional method is not acceptable, while the convergent and consistent hardness values were obtained from the modified method. For Cu films (0.002 s^{-1}), both methods returned similar results, except the hardness obtained by the conventional method is slightly larger than the modified method, and the convergence of the conventional method is slightly better than the modified method. This is because under the condition of a small load or small indentation depth, the determination of the contact area from only contact stiffness and load is less accurate than from contact stiffness, load, and indentation depth, despite the thermal drift.

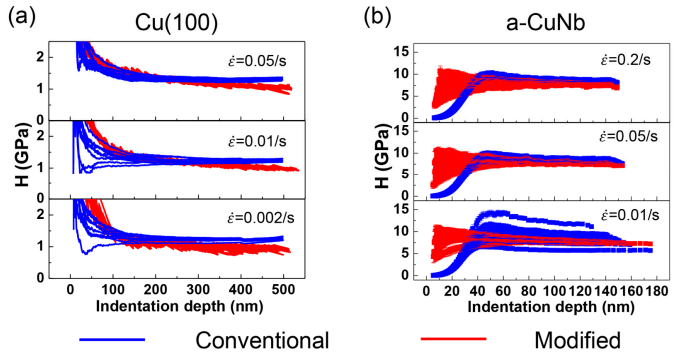

Figure 3. Comparison of nanoindentation results obtained from conventional (blue) and modified (red) methods using the same sets of indentation data at various strain rates for (**a**) Cu and (**b**) amorphous CuNb. At a high strain rate (0.05 s^{-1}), the indentation hardnesses calculated from both techniques are similar. However at low strain rate, the conventional analysis leads to more scattered results.

The SRS values of Cu film were calculated by using the hardness obtained at a depth of 300 nm from the two methods under different strain rates. As shown in Figure 4a, the SRS value (m = 0.048 $\pm$ 0.006) produced from the modified method (half-filled red circles) are less scattered than he conventional method. In contrast, the conventional method (half-filled black squares) leads to relatively erroneous and unacceptable SRS values (m = 0.112 $\pm$ 0.020), which are more than twice that of the modified method.

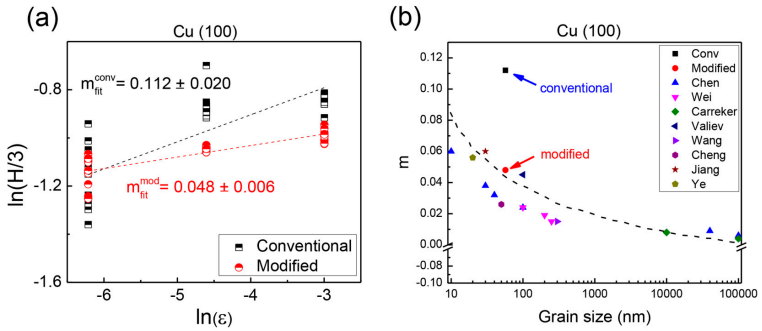

Figure 4. (**a**) The conventional method (half-filled black squares) yields erroneous SRS values for Cu. In contrast, the modified method (half-filled red circles) produces reliable SRS values. (**b**) Compiled plots of the SRS values (m) vs. grain size obtained from various techniques, including indentation jump, tensile and compression tests for Cu. The result obtained from the modified technique is consistent with the general trend reported in the literature, in contrast to the radically different result from the conventional method.

In order to further verify the reliability of the new method, we compare the measured SRS value of Cu film with the results that are obtained from bulk Cu samples or Cu films recorded in the previous literature, such as uniaxial tension, compression, and indentation jump tests [17–20,37–41], and plot the results in Figure 4b. For fcc metals, SRS normally increases with decreasing grain sizes. Here, the SRS value of Cu film with average grain size of ~70 nm (confirmed by TEM shown in Figure 5a) obtained from the modified technique is consistent with the general trend reported before, shown in Figure 4b. However, the conventional method shows very different results due to the influence of thermal drift at lower strain rates.

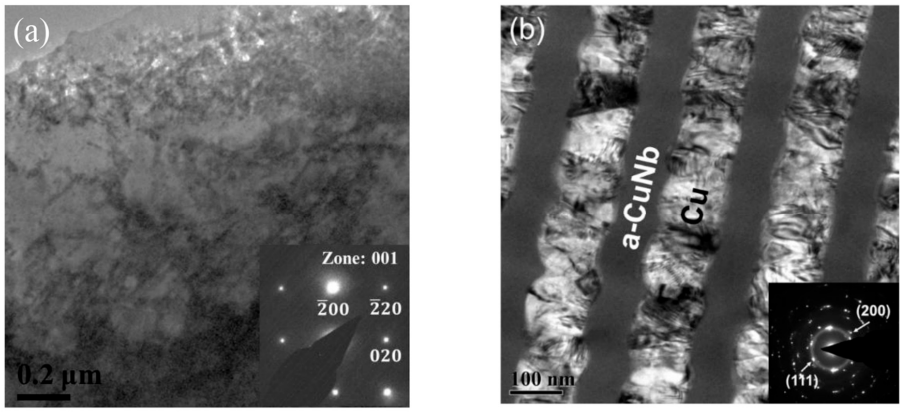

Figure 5. (**a**) Cross-section TEM micrograph of sputter-deposited nanocrystalline Cu film. (**b**) Cross-sectional TEM micrograph of sputter-deposited Cu 100 nm/a-CuNb 100 nm multilayer film.

After the new technique is validated through Cu films and returns expected SRS values, the SRS of C/A multilayers can be easily determined. Thus, in this section, the relationship between individual thickness (h), the plastic deformation mechanism, and the SRS of Cu/a-CuNb multilayers with different individual layer thickness (h, ranging from 5 to 150 nm) are systematically discussed. The image in Figure 5b is the cross-sectional microstructure of Cu 100 nm/a-CuNb 100 nm multilayers (referred as Cu/a-CuNb 100 nm) characterized by TEM. The layered structures can be clearly distinguished, and the selected area diffraction (SAD) pattern in the lower right corner shows diffuse diffraction halo and diffraction spots which represent the featureless amorphous layer and polycrystalline Cu layers, respectively.

Before conducting the nanoindentation experiments, we can briefly discuss the relationship between the SRS and individual layer thickness in crystalline (fcc metals)/amorphous multilayers. First, we assume that the C/A multilayers are under an isobaric stress condition during the nanoindentation experiment (i.e., the stress applied to crystalline layers and amorphous layers are equal). In this case, the total plastic deformation can be divided into two parts: the plastic deformation (strain) from the amorphous phase and from the crystalline phase. Moreover, the plastic deformation of these two phases is different partly due to the hardness of the amorphous phase being much higher than the crystalline phase. Thus, when the individual thickness of the amorphous phase and the crystalline phase are designed to the same value, the strain of C/A multilayers can be expressed as:

$$\varepsilon = \frac{1}{2}(\varepsilon_a + \varepsilon_c) \tag{4}$$

where ε is the total strain (indenter displacement divided by the film thickness: $\Delta L/L$), ε_a and ε_c are the strain of the amorphous layers and crystalline layers. Then, the strain rate can be shown as:

$$\dot{\varepsilon} = \frac{1}{2}(\dot{\varepsilon_a} + \dot{\varepsilon_c}) \tag{5}$$

Finally, according to [42], the SRS of C/A multilayers can be calculated as:

$$\frac{1}{m} = \frac{\partial \ln \dot{\varepsilon}}{\partial \ln \sigma} = \frac{\Delta L_a}{\Delta L_a + \Delta L_c} \times \frac{1}{m_a} + \frac{\Delta L_c}{\Delta L_a + \Delta L_c} \times \frac{1}{m_c} \quad (6)$$

where ΔL_a, m_a, ΔL_c, and m_c represent the displacement and SRS of the amorphous phase and the crystalline phase, respectively. Here, it is important to note that we should figure out the proportion of ε_a and ε_c in the total plastic deformation. That means the key in this study is to determine how the displacement is distributed. In Equation (6), both the SRS and the percentage of plastic deformation accommodated by the crystalline ($\frac{\Delta L_c}{\Delta L_a+\Delta L_c}$) and amorphous ($\frac{\Delta L_a}{\Delta L_a+\Delta L_c}$) layers should change with the change of h.

For the SRS of Cu/a-CuNb multilayers, we take the previously measured SRS of the 1.5 μm Cu film (m = 0.048, assuming that m does not change in this regime) into Equation (6) and treat m_a as a value close to zero, then we can qualitatively discuss the relationship between m and h. As shown in Figure 6a, the modeled curve (dashed line) indicates the evolution of co-deformation of both Cu and a-CuNb. In addition, the SRS of a-CuNb, Cu, their average value (dotted lines) and Cu/a-CuNb are also plotted on the graph.

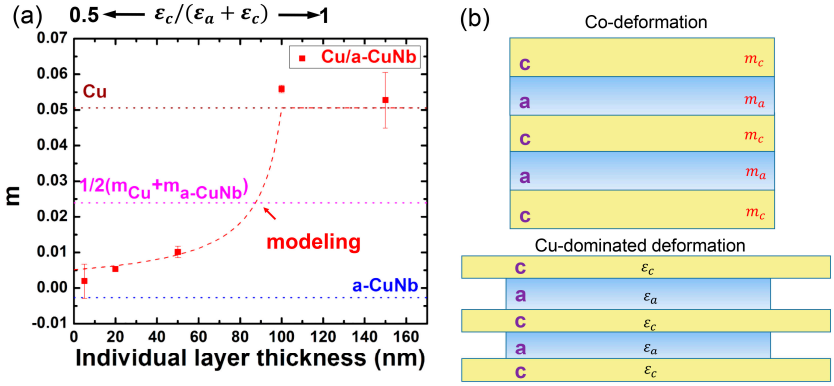

Figure 6. (**a**) SRS as a function of individual layer thickness (h) of Cu/a-CuNb multilayers. The SRS of a-CuNb, Cu, and their average values were added as dotted lines. When h < 50 nm, the SRS of Cu/a-CuNb multilayers decreases with decreasing h. When h > 100 nm, Cu/a-CuNb multilayers have an apparent SRS value similar to that of the single layer Cu film. The modeled curve (dashed line) indicates strain distribution from Cu and a-CuNb as a function of h. (**b**) A schematic showing the different deformation mechanisms at different h. When h is small (<50 nm), dislocation activities are limited and crystalline and amorphous layers can co-deform; when h is relatively large (>100 nm), deformation is dominated by dislocation activities, and crystalline layers accommodate more strain than amorphous layers.

The experimental data are consistent with the model discussed previously. At lager h, the plastic deformation is mainly generated by the crystalline phase, the value of $\frac{\Delta L_c}{\Delta L_a+\Delta L_c}$ will be close to 1 and $\frac{\Delta L_a}{\Delta L_a+\Delta L_c}$ close to zero. Therefore, the SRS should be similar to the single layer Cu. However, when h is smaller, the $\frac{\Delta L_c}{\Delta L_a+\Delta L_c}$ and $\frac{\Delta L_a}{\Delta L_a+\Delta L_c}$ would be close to 0.5 due to the co-deformation of crystalline phase and amorphous phase (the two phases share the deformation equally) [8,13], and the SRS would be closer to the single-layer amorphous film based on Equation (6).

Figure 6b is a schematic showing the different deformation mechanisms at different h. When h > 100 nm, Cu layers deform plastically due to its low strength and accommodate most of the strain, and thus Cu/a-CuNb multilayers have an apparent SRS value similar to that of the single layer Cu film. The mechanism of plastic deformation in this regime is dominated by dislocation activities inside the Cu layers.

When $h < 50$ nm, the SRS of Cu/a-CuNb multilayers decreases with decreasing h. The yield strength of Cu film increases with decreasing h due to the Hall-Petch effect (although there may occasionally be an inverse Hall-Petch effect when the grain size decreases to a few nanometers, here we leave this possibility aside). At the same time, the density of dislocations in the Cu grains decreases and the activation volume increases. The generation and propagation of dislocation is very difficult, and the stress concentration caused by the dislocations at the interface is not enough to transmit the dislocations across the interface. The limited dislocations will be confined within the Cu layers and slide along the interface [43]. On the other hand, for the a-CuNb layers, the deformation mechanism is the coalescence of shear transformation zones instead of major shear banding, and at this layer thickness, Cu and a-CuNb layers can co-deform.

4. Conclusions

A new nanoindentation test method that enables reliable determination of SRS is reviewed. The new method is applied in two model systems (single-layer Cu film and Cu/amorphous-CuNb multilayers) to reduce the thermal drift effect and yields reliable results. The method yields correct SRS of single-layer Cu film compared with the conventional method, and the layer thickness-dependent SRS of Cu/a-CuNb nanolayers under the iso-stress condition is systematically discussed: when $h > 100$ nm, the plastic deformation is mainly accommodated by the Cu layers through dislocation pile-up, and Cu/a-CuNb multilayers have an apparent SRS value similar to that of the single layer Cu film; when $h < 50$ nm, the crystalline and amorphous layers co-deform, and the SRS of Cu/a-CuNb multilayers decreases with decreasing h. The main deformation mechanism is interface-mediated. This new method is beneficial for the measurement of hardness and the SRS of nano-scale materials without the thermal drift error at low strain rate under nanoindentation.

Acknowledgments: X.Z. acknowledges the partial financial support by NSF-DMR 1642759.

Author Contributions: Y.L. and X.Z. conceived and designed the experiments; Y.L. and Z.F. performed the experiments; Z.F. and J.S. analyzed the data; J.S. wrote the paper.

Conflicts of Interest: The authors declare no conflict of interest.

References

1. Suo, T.; Ming, L.; Zhao, F.; Li, Y.L.; Fan, X. Temperature and strain rate sensitivity of ultrafine-grained copper under uniaxial compression. *Int. J. Appl. Mech.* **2013**, *5*, 1350016. [CrossRef]
2. Asaro, R.J.; Suresh, S. Mechanistic models for the activation volume and rate sensitivity in metals with nanocrystalline grains and nano-scale twins. *Acta Mater.* **2005**, *53*, 3369–3382. [CrossRef]
3. Wei, Q. Strain rate effects in the ultrafine grain and nanocrystalline regimes—Influence on some constitutive responses. *J. Mater. Sci.* **2007**, *42*, 1709–1727. [CrossRef]
4. Akihisa, I. Stabilization of metallic supercooled liquid and bulk amorphous alloys. *Acta Mater.* **2000**, *48*, 279–306.
5. Greer, A.L.; Cheng, Y.Q.; Ma, E. Shear bands in metallic glasses. *Mater. Sci. Eng. R Rep.* **2013**, *74*, 71–132. [CrossRef]
6. Hofmann, D.C.; Suh, J.Y.; Wiest, A.; Duan, G.; Lind, M.L.; Demetrious, M.D.; Johnson, W.L. Designing metallic glass matrix composites with high toughness and tensile ductility. *Nature* **2008**, *451*, 1085–1089. [CrossRef] [PubMed]
7. Knorr, I.; Cordero, N.M.; Lilleodden, E.T.; Volkert, C.A. Mechanical behavior of nanoscale Cu/PdSi multilayers. *Acta Mater.* **2013**, *61*, 4984–4995. [CrossRef]
8. Zhang, J.Y.; Liu, Y.; Chen, J.; Chen, Y.; Liu, G.; Zhang, X.; Sun, J. Mechanical properties of crystalline Cu/Zr and crystal–amorphous Cu/Cu–Zr multilayers. *Mater. Sci. Eng. A* **2012**, *552*, 392–398. [CrossRef]
9. Chu, J.P.; Jang, J.S.C.; Huang, J.C.; Chou, H.S.; Yang, Y.; Ye, J.C.; Wang, Y.C.; Lee, J.W.; Liu, F.X.; Liaw, P.K.; et al. Thin film metallic glasses: Unique properties and potential applications. *Thin Solid Films* **2012**, *520*, 5097–5122. [CrossRef]

10. Huang, L.; Zhou, J.; Zhang, S.; Wang, Y.; Liu, Y. Effects of interface and microstructure on the mechanical behaviors of crystalline Cu-amorphous Cu/Zr nanolaminates. *Mater. Des.* **2012**, *36*, 6–12. [CrossRef]
11. Fan, Z.; Xue, S.; Wang, J.; Yu, K.Y.; Wang, H.; Zhang, X.H. Unusual size dependent strengthening mechanisms of Cu/amorphous CuNb multilayers. *Acta Mater.* **2016**, *120*, 327–336. [CrossRef]
12. Wang, Y.M.; Li, J.; Hamza, A.V.; Barbee, T.W., Jr. Ductile crystalline-amorphous nanolaminates. *Proc. Natl. Acad. Sci. USA* **2007**, *104*, 11155–11160. [CrossRef] [PubMed]
13. Kim, J.Y.; Jang, D.C.; Greer, J.R. Nanolaminates utilizing size-dependent homogeneous plasticity of metallic glasses. *Adv. Funct. Mater.* **2011**, *21*, 4550–4554. [CrossRef]
14. Donohue, A.; Spaepen, F.; Hoagland, R.G.; Misra, A. Suppression of the shear band instability during plastic flow of nanometer-scale confined metallic glasses. *Appl. Phys. Lett.* **2007**, *91*, 241905. [CrossRef]
15. Torre, F.D.; Swygenhoven, H.V.; Victoria, M. Nanocrystalline electrodeposited Ni: Microstructure and tensile properties. *Acta Mater.* **2002**, *50*, 3957–3970. [CrossRef]
16. Lu, L.; Li, S.X.; Lu, K. An abnormal strain rate effect on tensile behavior in nanocrystalline copper. *Scr. Mater.* **2001**, *45*, 1163–1169. [CrossRef]
17. Valiev, R.Z.; Alexandrov, I.V.; Zhu, Y.T.; Lowe, T.C. Paradox of strength and ductility in metals processed by severe plastic deformation. *J. Mater. Res.* **2011**, *17*, 5–8. [CrossRef]
18. Wang, Y.M.; Ma, E. Temperature and strain rate effects on the strength and ductility of nanostructured copper. *Appl. Phys. Lett.* **2003**, *83*, 3165–3167. [CrossRef]
19. Wei, Q.; Cheng, S.; Ramesh, K.T.; Ma, E. Effect of nanocrystalline and ultrafine grain sizes on the strain rate sensitivity and activation volume: fcc versus bcc metals. *Mater. Sci. Eng. A* **2004**, *381*, 71–79. [CrossRef]
20. Gu, C.D.; Lian, J.S.; Jiang, Z.H.; Jiang, Q. Enhanced tensile ductility in an electrodeposited nanocrystalline Ni. *Scr. Mater.* **2006**, *54*, 579–584. [CrossRef]
21. May, J.; Höppel, H.W.; Göken, M. Strain rate sensitivity of ultrafine-grained aluminium processed by severe plastic deformation. *Scr. Mater.* **2005**, *53*, 189–194. [CrossRef]
22. Li, Y.J.; Mueller, J.; Höppel, H.W.; Göken, M.; Blum, W. Deformation kinetics of nanocrystalline nickel. *Acta Mater.* **2007**, *55*, 5708–5717. [CrossRef]
23. Lucas, B.N.; Oliver, W.C. Indentation power-law creep of high purity indium. *Metall. Mater. Trans. A* **1999**, *30A*, 601–610. [CrossRef]
24. Hay, J.; Agee, P.; Herbert, E. Continuous stiffness measurement during instrumented indentation testing. *Exp. Tech.* **2010**, *34*, 86–94. [CrossRef]
25. Maier, V.; Durst, K.; Mueller, J.; Backes, B.; Höppel, H.W.; Göken, M. Nanoindentation strain-rate jump tests for determining the local strain-rate sensitivity in nanocrystalline Ni and ultrafine-grained Al. *J. Mater. Res.* **2011**, *26*, 1421–1430. [CrossRef]
26. Liu, Y.; Bufford, D.; Wang, H.; Sun, C.; Zhang, X.H. Mechanical properties of highly textured Cu/Ni multilayers. *Acta Mater.* **2011**, *59*, 1924–1933. [CrossRef]
27. Liu, Y.; Bufford, D.; Rios, S.; Wang, H.; Chen, J.; Zhang, J.Y.; Zhang, X. A formation mechanism for ultra-thin nanotwins in highly textured Cu/Ni multilayers. *J. Appl. Phys.* **2012**, *111*, 073526. [CrossRef]
28. Liu, Y.; Chen, Y.; Yu, K.Y.; Wang, H.; Chen, J.; Zhang, X. Stacking fault and partial dislocation dominated strengthening mechanisms in highly textured Cu/Co multilayers. *Int. J. Plast.* **2013**, *49*, 152–163. [CrossRef]
29. Hasnaoui, A.; Derlet, P.M.; Van Swygenhoven, H. Interaction between dislocations and grain boundaries under an indenter—A molecular dynamics simulation. *Acta Mater.* **2004**, *52*, 2251–2258. [CrossRef]
30. Voyiadjis, G.Z.; Yaghoobi, M. Review of nanoindentation size effect: Experiments and atomistic simulation. *Crystals* **2017**, *7*, 321. [CrossRef]
31. Voyiadjis, G.Z.; Yaghoobi, M. Role of grain boundary on the sources of size effects. *Comput. Mater. Sci.* **2016**, *117*, 315–329. [CrossRef]
32. Nair, A.K.; Parker, E.; Gaudreau, P.; Farkas, D.; Kriz, R.D. Size effects in indentation response of thin films at the nanoscale: A molecular dynamics study. *Int. J. Plast.* **2008**, *24*, 2016–2031. [CrossRef]
33. Liu, Y.; Hay, J.; Wang, H.; Zhang, X.H. A new method for reliable determination of strain-rate sensitivity of low-dimensional metallic materials by using nanoindentation. *Scr. Mater.* **2014**, *77*, 5–8. [CrossRef]
34. Sneddon, I.N. The relation between load and penetration in the axisymmetric boussinesq problem for a punch of arbitrary profile. *Int. J. Eng. Sci.* **1965**, *3*, 47–57. [CrossRef]
35. Oliver, W.C.; Pharr, G.M. An improved technique for determining hardness and elastic modulus using load and displacement sensing indentation experiments. *J. Mater. Res.* **2011**, *7*, 1564–1583. [CrossRef]

36. Pharr, G.M.; Oliver, W.C.; Brotzen, F.R. On the generality of the relationship among contact stiffness, contact area, and elastic modulus during indentation. *J. Mater. Res.* **2011**, *7*, 613–617. [CrossRef]
37. Cheng, S.; Ma, E.; Wang, Y.M.; Kecskes, L.J.; Youssef, K.M.; Koch, C.C.; Trociewitz, U.P.; Han, K. Tensile properties of in situ consolidated nanocrystalline Cu. *Acta Mater.* **2005**, *53*, 1521–1533. [CrossRef]
38. Gray, G.T., III; Lowe, T.C.; Cady, C.M.; Vaile, R.Z.; Aleksandrov, I.V. Influence of strain rate & temperature on the mechanical response of ultrafine-grained Cu, Ni, and Al-4Cu-0.5Zr. *Nanostruct. Mater.* **1997**, *9*, 477–480.
39. Chen, J.; Lu, L.; Lu, K. Hardness and strain rate sensitivity of nanocrystalline Cu. *Scr. Mater.* **2006**, *54*, 1913–1918. [CrossRef]
40. Jiang, Z.H.; Liu, X.L.; Li, G.Y.; Jiang, Q.; Lian, J.S. Strain rate sensitivity of a nanocrystalline Cu synthesized by electric brush plating. *Appl. Phys. Lett.* **2006**, *88*, 143115. [CrossRef]
41. Ye, J.C.; Wang, Y.M.; Barbee, T.W.; Hamza, A.V. Orientation-dependent hardness and strain rate sensitivity in nanotwin copper. *Appl. Phys. Lett.* **2012**, *100*, 261912. [CrossRef]
42. Fan, Z.; Liu, Y.; Xue, S.; Rahimi, R.M.; Bahr, D.F.; Wang, H.; Zhang, X. Layer thickness dependent strain rate sensitivity of Cu/amorphous CuNb multilayer. *Appl. Phys. Lett.* **2017**, *110*, 161905. [CrossRef]
43. Misra, A.; Hirth, J.P.; Hoagland, R.G. Length-scale-dependent deformation mechanisms in incoherent metallic multilayered composites. *Acta Mater.* **2005**, *53*, 4817–4824. [CrossRef]